Available online at www.sciencedirect.com
ScienceDirect
C. R. Physique 8 (2007) 288–297
COMPTES RENDUS PHYSIQUE
http://france.elsevier.com/direct/COMREN/

Optical techniques for direct imaging of exoplanets/Techniques optiques pour l'imagerie directe des exoplanètes

Band-limited masks for TPF coronagraph

Kunjithapatham Balasubramanian *, Erkin Sidick, Daniel W. Wilson, Daniel J. Hoppe, Stuart B. Shaklan, John T. Trauger

Jet Propulsion Laboratory, California Institute of Technology, 4800 Oak Grove Drive, Pasadena, CA 91109, USA

Available online 6 June 2007

Abstract

Band-limited image plane masks, in conjunction with appropriate Lyot stops, function effectively to suppress host star light while transmitting planet light to the final image for detecting and characterizing faint exo-solar terrestrial planets. In this article, we review various types of image plane masks, their design, fabrication, and characterization. Measured characteristics and performance of sample masks in simulations and in laboratory experiments are also discussed. Star light suppression contrast better than 10^{-9} in the 4 to 10 λ/D region has been demonstrated with such a mask in our laboratory testbed. ***To cite this article: K. Balasubramanian et al., C. R. Physique 8 (2007).***

Résumé

Masques à spectre limité pour le coronographe de TPF. Les masques à bande limitée associés à des Lyot stops convenables peuvent supprimer efficacement la lumière de l'étoile pour permettre l'observation de l'exoplanète et son analyse. Dans cet article, nous présentons une revue de différents types de masques, leur conception, leur réalisation et leurs tests. Nous donnons les caractéristiques mesurées et les performances des masques testés en laboratoire et par simulation numérique. Une suppression de la lumière meilleure que 10^{-9} dans la région de 4 à 10 λ/D a été démontrée avec de tels masques dans notre banc d'essai de laboratoire. ***Pour citer cet article : K. Balasubramanian et al., C. R. Physique 8 (2007).***

Keywords: TPF coronagraph; Occulting mask; Band-limited mask; HCIT

Mots-clés : Coronographe TPF ; Masques occulteurs ; Masque à bande limité ; Banc ITHD

1. Introduction

Detecting and characterizing exo-solar terrestrial planets which are 10^{10} times fainter than their parent stars present interesting engineering challenges. Central to the instrument that would enable observation and characterization of exo-solar planets in the visible spectrum is a star light suppression system with appropriate masking techniques. Occulting focal plane masks [1] operate in conjunction with a Lyot stop to suppress the on-axis starlight in a coronagraphic telescope. Fig. 1 shows a conceptual drawing of a classical coronagraph with a focal plane mask and a Lyot stop. In the limit of Fourier optics [2], these masks can be designed to reject the starlight in the regions of interest to

* Corresponding author.
E-mail address: kbala@jpl.nasa.gov (K. Balasubramanian).

1631-0705/$ – see front matter
doi:10.1016/j.crhy.2007.03.001

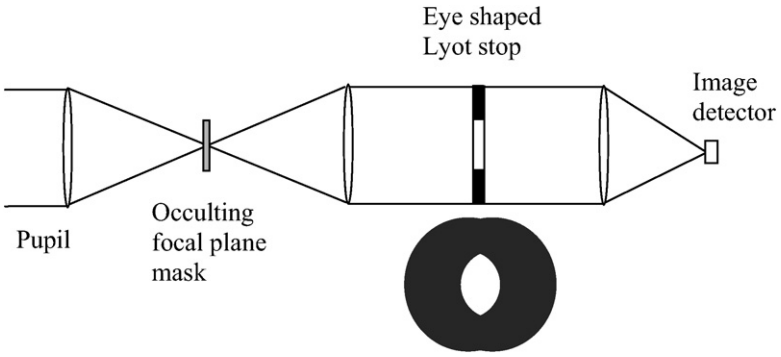

Fig. 1. Conceptual diagram [8] of a coronagraph with a focal plane mask and a Lyot stop.

below 10^{-10}, the nominal Terrestrial Planet Finder (TPF) requirement [3,4]. Gray scale and equivalent binary masks can be designed to meet such a requirement.

Although traditional graded occulting masks, such as those with a Gaussian profile, can be used with an appropriate Lyot stop to suppress starlight, operation close to a few diffraction widths of the optical axis requires a relatively small low-throughput stop. However, if the mask transmission profile is chosen from functions that are both zero on axis and have a band-limited transform, it is possible to completely eliminate the diffracted starlight from reaching the final image with a high-throughput Lyot stop [1]. It has been shown that if we further restrict the set of functions to those that have a vanishing second derivative on axis, we can improve upon the nominal 4th order pointing error sensitivity of a band-limited mask and obtain a more desirable 8th order sensitivity [5,6]. In general, an nth order mask is one in which the intensity transmission varies as the nth power of the distance from the optical axis in the proximity of the axis. The band-limited masks designed to be symmetric about the optical axis have mask functions of even orders. Some examples of image plane masks are:

(a) Continuous gray scale 4th and 8th order band-limited masks;
(b) Notch filter type masks—binary variations;
(c) Discontinuous/stepped gray scale masks.

Such band-limited image plane masks have been proposed for space borne coronagraph instruments for exoplanet detection and observation [7,1]. Different types of these masks have been designed and fabricated for laboratory tests [8,9] at JPL as described below.

2. Masks

2.1. Gray scale image plane masks

One- and two-dimensional analog gray scale masks of the $1 - \text{sinc}^2$ type with transmittance T given by $T = [1 - \text{sinc}^2]^2$ can be designed as shown in Fig. 2. Here the sinc function is defined as $[\sin(\pi x)]/\pi x$ for the one-dimensional case. As suggested by Kuchner and Spergel [10], one-dimensional masks have certain advantages such as ease of manufacturing, convenience to translate the mask to its best location relative to errors, and better throughput of planet light, though with a reduced search space.

Gray scale masks can be fabricated with a high energy electron beam sensitive glass called HEBS glass [11]. One-dimensional $1 - \text{sinc}^2$ type 4th order masks have been fabricated at JPL with such a glass to enable experiments in the High Contrast Imaging Testbed (HCIT). Normally transparent HEBS glass becomes dark when exposed to a high energy electron beam. The resulting transmittance or optical density (OD) is a function of the electron beam energy and dosage. Employing 100 KeV electron beams in an e-beam lithography system at JPL, HEBS glass based occulting masks have been fabricated and tested. We discuss the simulation and experimental results with these masks below.

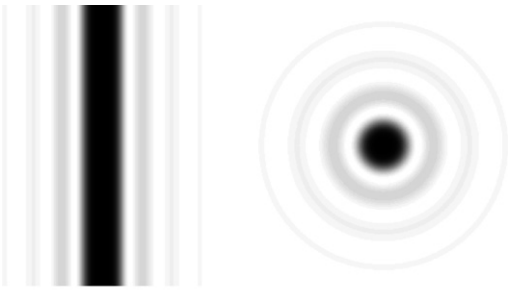

Fig. 2. Conceptual transmission images of the inner region of (a) one- and (b) two-dimensional gray scale $1 - \text{sinc}^2$ type masks.

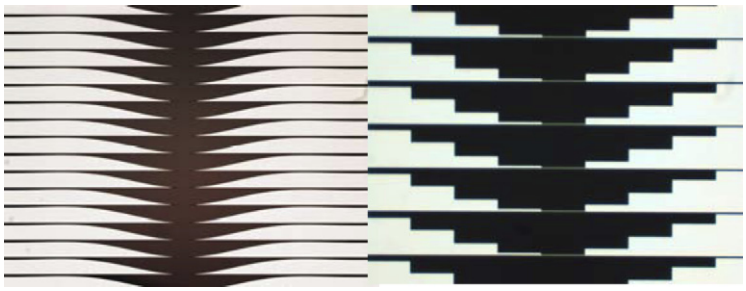

Fig. 3. Examples of continuous binary mask and sampled binary mask.

2.2. Binary masks

Binary masks with opaque and transparent patterns designed to mimic effectively the profile of analog gray scale masks can also be designed and fabricated. In the case of binary masks, an analog band-limited function such as $\sin^2$ or $1 - \text{sinc}^2$ is sampled and a series of apertures is created that resembles the transmission of the analog mask. 'Continuous' and 'sampled' $\sin^2$ and $1 - \text{sinc}^2$ type masks as shown in Fig. 3 have been designed and fabricated [8]. Here 'sampled' refers to the fine discrete steps making up an otherwise continuous profile.

Fig. 4 shows a close-up view [8] of a fabricated 'continuous' $1 - \text{sinc}^2$ type binary mask. It is designed to mimic the $1 - \text{sinc}^2$ transmission profile of the HEBS mask. The mask is referred to as binary since it consists only of perfectly blocking metal and totally transmitting empty apertures (0/1). In general, if the parent function is periodic, then the resulting binary mask will also be periodic in the search direction (x). If the parent function is non-periodic, such as $1 - \text{sinc}^2$, then the binary mask is non-periodic in the search direction. Unlike gray scale masks, both periodic and non-periodic types of binary masks are chosen to be periodic in the non-search direction (y), with a period of $F\# * \lambda$, where $F\#$ is the focal length/diameter ratio of the telescope and λ is the operating wavelength. Fig. 4 shows a periodic pattern in y direction with a non-periodic $1 - \text{sinc}^2$ pattern in x. The dimensions of these patterns along with the appropriately chosen Lyot stop dimensions insure that the diffraction from this periodic structure falls outside the Lyot stop. Typical inner working angle (IWA) values are in the range of 3–5 (λ/D) for the TPF mission. To match with the performance of our gray scale HEBS mask designs, binary masks were designed for the same $F\#$ and wavelength. The binary mask patterns are generated by e-beam lithography and lift off process with nominally 200 nm thick aluminum film coated by evaporation on fused silica glass.

2.3. Fourth, eighth and higher order masks

Band-limited $1 - \text{sinc}^2$ type masks have a 4th order sensitivity to tip/tilt while the 8th order masks [5] have 8th order dependence. The low order aberration sensitivity of 4th and 8th order masks have been analyzed in detail [5,6]. 8th order masks on HEBS glass were fabricated along with 4th order masks; initial tests show that they perform similar

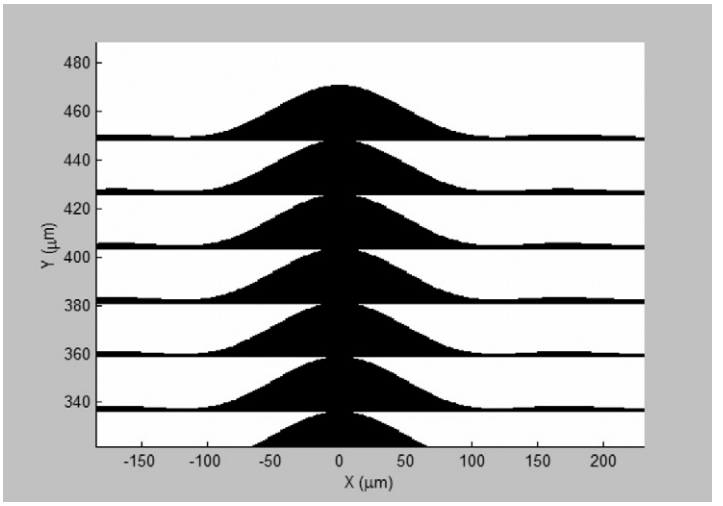

Fig. 4. Close-up view of a one-dimensional binary $1 - \text{sinc}^2$ type mask pattern [8]; black areas are made of perfectly opaque and etched metal layer.

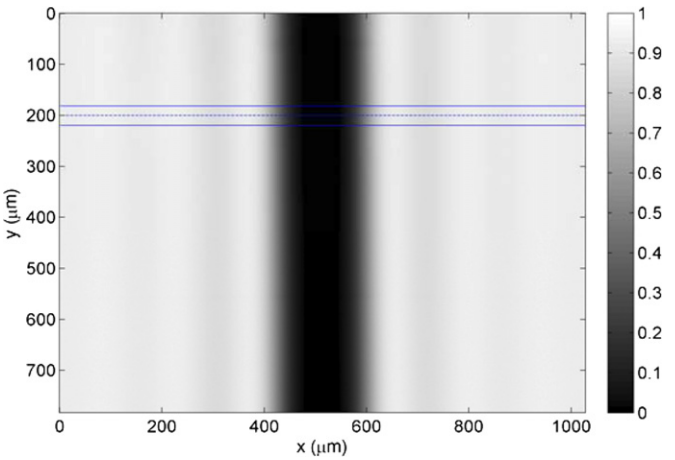

Fig. 5. Measured intensity-transmission image of a $1 - \text{sinc}^2$ type one-dimensional gray scale mask fabricated at JPL. Lines indicate the region of profile averaging for cross-section data shown in Fig. 6.

to 4th order masks for monochromatic contrast in the test bed. Crepp et al. [12] have recently reported theoretical estimates of sensitivities and laboratory measurements of contrast with 8th order masks.

3. Practical gray scale image masks, HCIT simulations and modeling results

Image plane masks fabricated by electron beam exposure of HEBS glass have provided satisfactory contrast performance with laser light in the HCIT. However, they suffer from wavelength dependent optical density (OD) and OD-dependent transmitted phase, rendering them non-bandlimited. Their actual performance in HCIT is thus limited, particularly with broadband light. Our understanding of these masks based on measurements and simulations is discussed below.

The transmittance profiles, i.e., OD versus x coordinate of the fabricated one-dimensional occulting masks, were measured using a transmission imaging microscope [13]. One such transmittance image is shown in Fig. 5 for the $1 - \text{sinc}^2$ type mask examined in further detail in this article. The measured occulting mask profile used in the analysis was a 50-row average cross-section of the image as shown in Fig. 6.

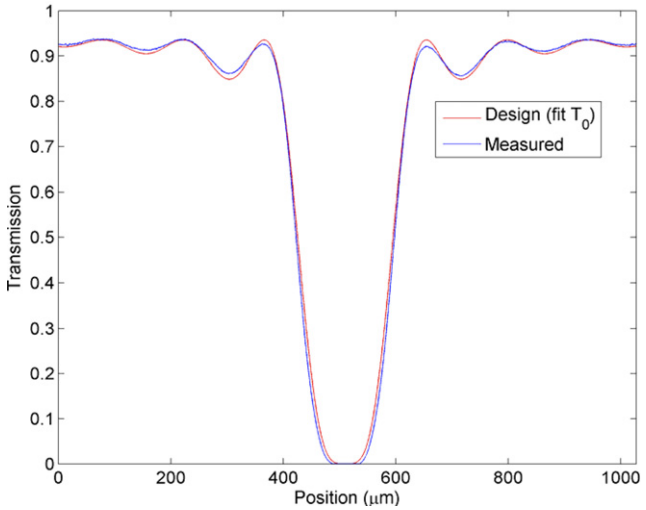

Fig. 6. Cross-section profile of $1 - \text{sinc}^2$ mask (50-row average between lines in Fig. 5) [13]. A fit of the design function $T(x) = T_0[1 - \text{sinc}^2(x/w)]^2$ with maximum transmittance $T_0 = 0.935$ as a parameter is shown for comparison.

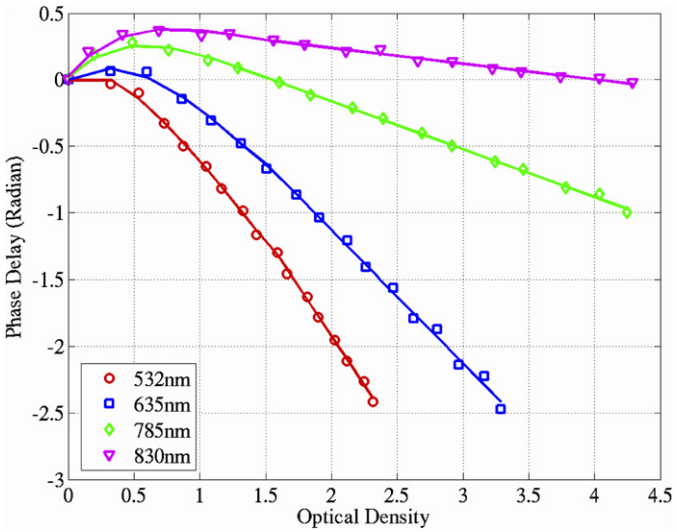

Fig. 7. HEBS mask phase delay as a function of OD with wavelength as a parameter. The symbols represent the measured data [14] of a HEBS glass and the corresponding curves were obtained from an analytical model fit [13] of the measured data, $\phi = \phi(\text{OD}, \lambda)$.

Similarly, the phase of transmitted light through a calibration sample with many steps of OD was measured with an interferometer system [14]. The measured phase versus OD data used in the current analysis is shown in Fig. 7 with different symbols representing the four different measurement wavelengths. The solid-curves in Fig. 7 were obtained using an analytical model of measured data while the measured data are shown by symbols. Note that the phase ϕ here refers to the phase difference between a region of known OD to a transparent or bias region outside of the mask area. An ideal occulter is expected to have zero phase versus OD, i.e., the phase should be constant over the entire mask. We have developed an analytical model for this type of occulter phase in practical masks in the form of $\phi = \phi(\text{OD}, \lambda)$, and used it to obtain the occulter phase information at different wavelengths and at regions where $\text{OD} > 4.5$ for which measurements could not be made. As we can see from Fig. 7, there are two distinctive regions in each $\phi(\text{OD}, \lambda)$ curve: A nonlinear region at $\text{OD} < 1.5$, and a linear region at $1.5 \leqslant \text{OD} < 4.5$. The occulter phase is not important when $\text{OD} \geqslant 8$ and we assume $\phi(\text{OD} > 8, \lambda) = \phi(\text{OD} = 8, \lambda)$ for that region in our simulations. Fig. 8 shows the OD

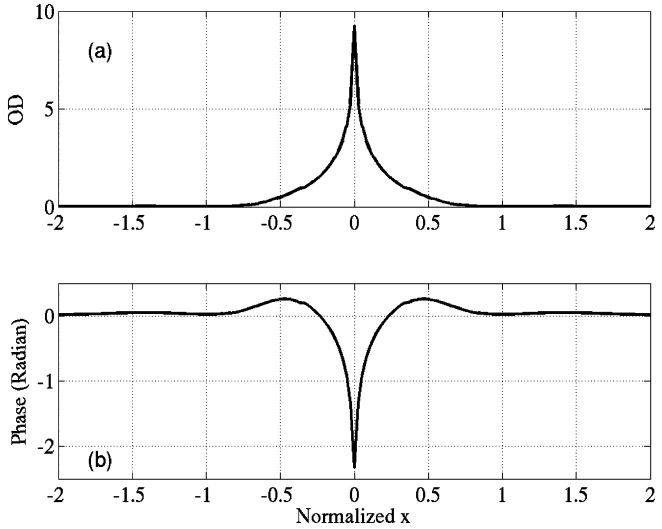

Fig. 8. OD and phase profiles of a linear (one-dimensional) $1 - \mathrm{sinc}^2$ occulting mask [13]. (a) OD profiles measured at $\lambda = 785$ nm; (b) corresponding phase profile obtained from the analytical model fit of measured data $\phi = \phi(\mathrm{OD}, \lambda)$. In the figure, normalized x refers to x/w.

and the phase profiles of an occulter, where the OD curve represents the data measured at $\lambda = 785$ nm, and the phase curve for $\lambda = 785$ nm was obtained from the analytical model fit $\phi = \phi(\mathrm{OD}, \lambda)$ of measured data described above.

Here, we briefly describe the difference of the measured occulter OD profile from the original design profile. The test setup used to measure the OD profiles of gray-scale occulting masks studied here had a noise floor of OD ~ 3. It was found that the measured OD profile deviates from the design starting at OD ≈ 1, and such deviation becomes increasingly prominent starting at OD > 3. Therefore, for simulations, the measured OD values in Fig. 8(a) corresponding to OD > 1 were replaced by the data calculated from the design transmittance profile,

$$T(x) = \left[1 - \left(\frac{\sin(\pi x/w)}{(\pi x/w)}\right)^2\right]^2 \tag{1}$$

with $w = 144.0$ μm, where w is the occulter width. The thus modified measured profile is referred to as 'measured' in the following discussion. The original design had $w = 141.9$ μm. That is, the fabricated occulter turned out to be slightly wider than the original target design. In addition, a close examination of the measured OD profile reveals that it differs from the design in the following two additional aspects: (i) Its sinusoidal ripples are damped (or smoothed) and do not hit the OD $= 0$ axis, as shown in Fig. 9(a). This might have been caused mostly by fabrication errors, and to a less extent by measurement errors; (ii) The measured OD versus x curve rises faster than the target at $0.35 < x/w < 0.7$, as shown in Fig. 9(b). The discontinuity on the 'measured' curve in Fig. 9(b) near $x/w \sim 0.35$ is caused by the mismatch between the measured data and the model.

4. Experimental results

4.1. Experimental results with a practical gray scale mask

The HEBS and binary masks described above were tested for performance in the HCIT at JPL. The testbed set up has been described by Trauger et al. [9]. A recent addition to the test bed optics is a calcite polarizer before the final image detector to separate the two orthogonally polarized images into non-overlapping locations at the final image plane. The deformable mirror (DM) in the testbed can be optimized to minimize the speckles in either polarization independently, thus estimating the best contrast achievable in one polarization while allowing the other to float. While the HEBS gray scale mask does not exhibit polarization sensitivity, the binary mask is inherently sensitive to polarization. Both HEBS and binary masks were mounted side by side to facilitate the use of either mask by external control without breaking vacuum and to ensure nearly identical conditions for the two masks during the tests.

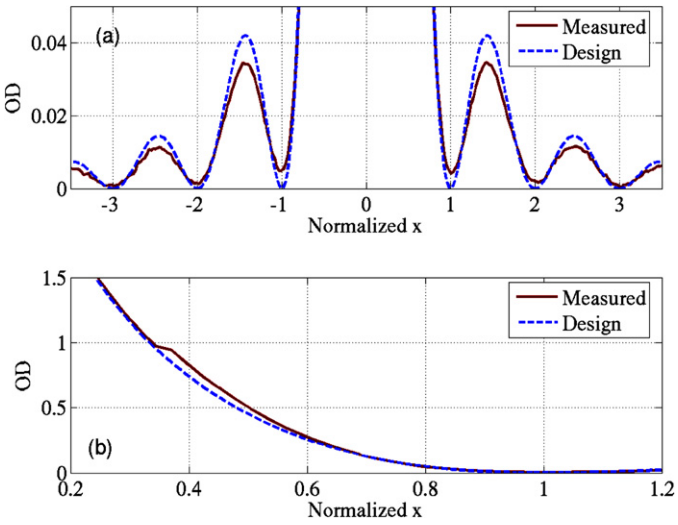

Fig. 9. Comparison of the 'measured' and the 'design' OD profiles of a linear $1 - \text{sinc}^2$ occulting mask [13] designed with $w = 141.9$ μm. In the figure, normalized x refers to x/w. (a) The ripples of the measured OD profile are smoothed (or damped) as compared to the design; (b) In regions where $0.3 < |x/w| < 1$, the measured OD profile deviates from the standard $1 - \text{sinc}^2$ design.

Mask fabrication, testbed optics and nulling techniques are under progressive development at JPL with significant improvements. Speckle-nulling experiments are conducted in the HCIT with gray scale and binary masks. Coronagraphic images are obtained with a HEBS gray scale $1 - \text{sinc}^2$ linear occulting mask with a 785 nm laser source. We use a mean contrast, C_m, and a contrast at 4 λ/D, C_4, as the metrics of the HCIT's performance. Here, the C_m is defined as the contrast value averaged over the rectangular window defined by $[4 \leqslant x \leqslant 10, -10 \leqslant y \leqslant 10] * \lambda f/D$, and the C_4 as the one averaged over a smaller window of $[4 \leqslant x \leqslant 5, -0.5 \leqslant y \leqslant 0.5] * \lambda f/D$. In an experiment conducted with a HEBS gray scale mask in 2005 [8], we obtained $C_m \sim 9 \times 10^{-10}$ with a stability of about 0.5×10^{-10} per hour. In a more detailed study [15] conducted in 2006, we obtained $C_m \sim 6 \times 10^{-10}$ in a nulling window defined by a 'D' shaped region covering 4 to 10 λ/D. Reproducibility of this contrast pattern (i.e., drift plus noise) was about 0.1×10^{-10} over a 5 hour period.

4.2. Experimental results with a practical binary mask

A binary $1 - \text{sinc}^2$ type mask was tested in the HCIT under similar conditions as with the HEBS mask. With incident 785 nm unpolarized laser light split into orthogonal polarizations after the mask and before the final image, an average contrast of $\sim 4 \times 10^{-9}$ was obtained in the rectangular target region for a chosen polarization that was nulled with the DM while the other polarization was left floating. Images corresponding to the two polarizations [8] are shown as insets in Figs. 10(a) and 10(b) where contrast values are plotted for various radial locations from 4 to 14 λ/D. Theoretical simulations using full-wave electromagnetic models of the gap behavior [4] and Fresnel diffraction compare closely with the experimental results; observed differences between theory and experiment, particularly with respect to polarization behavior of binary masks, could be explained as due to model assumptions and experimental conditions.

5. Broadband modeling

The performance described above demonstrates that high contrast is obtained in monochromatic light when the DM is used to compensate for all the system errors including mask OD and phase errors. Ultimately, however, the masks must be used in broadband light ($\sim$100 nm bandwidth) to see exo-solar terrestrial planets. Here we show, as also discussed in detail elsewhere [13], how the performance of the gray scale masks detailed in Figs. 6 to 9 (cross-section figure and phase vs. OD versus wavelength figure) degrades as a function of bandwidth.

Fig. 11 (a) and (b) show C_m and C_4 as a function of bandwidth around 785 nm center wavelength. The wavelength-dependence occulter phase and the phases of all the optics are included in this simulation; however, the wavelength

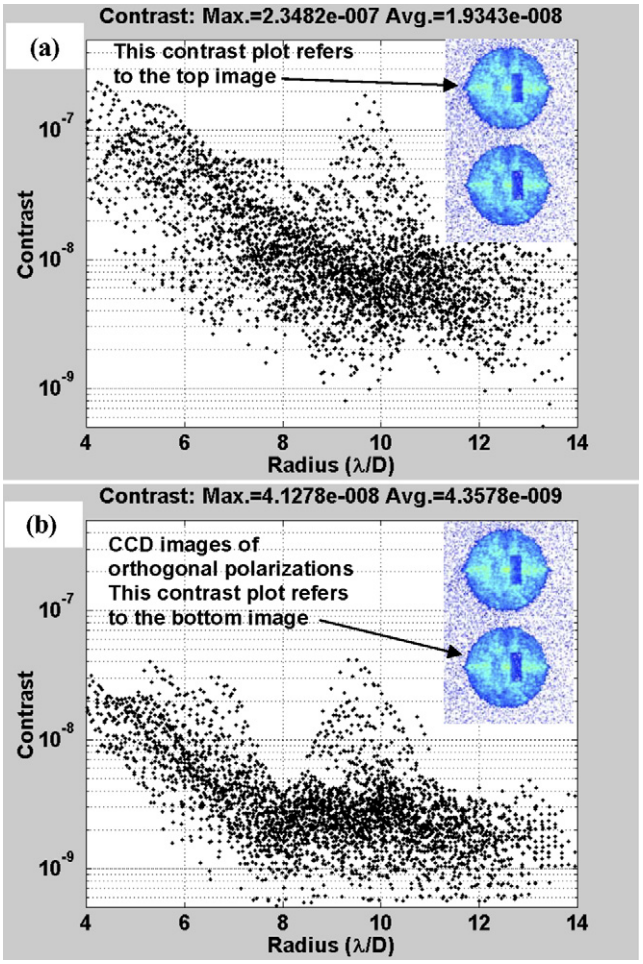

Fig. 10. Final images (insets in the figures) showing the two polarizations and the corresponding contrast plots from experimental data with binary mask [8]. Top (a): Contrast plot of polarization not being nulled by DM. The average is 1.9×10^{-8}. Bottom (b): Contrast plot of polarization being nulled by DM. The average is 4.3×10^{-9}.

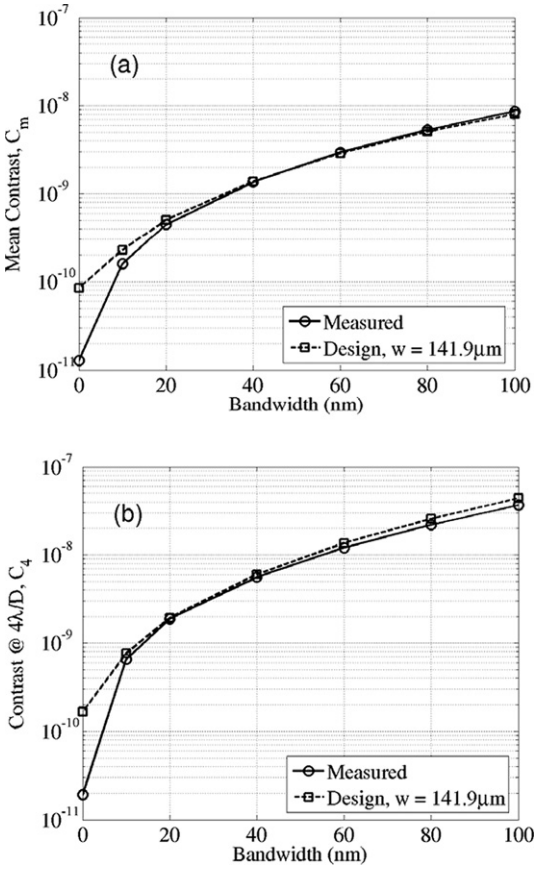

Fig. 11. Theoretical broadband contrast as a function of bandwidth $\Delta\lambda$ around 785 nm center wavelength. The curves marked as 'Measured' and 'Design' $w = 141.9$ μm correspond to the occulter OD profiles illustrated in Fig. 9. (a) Mean contrast, C_m, averaged over the rectangular window defined by $[4 \leqslant x \leqslant 10, -10 \leqslant y \leqslant 10] * \lambda f/D$, and (b) contrast at 4 λ/D, C_4 averaged over a smaller window of $[4 \leqslant x \leqslant 5, -0.5 \leqslant y \leqslant 0.5] * \lambda f/D$.

dependent of OD which was measured to be small in this bandwidth, is not included. The DM settings used are those obtained for the 785 nm wavelength in each case. That is, this figure shows how the HCIT is expected to perform with a broadband light beam when the DM is kept at a setting optimized for the (monochromatic) central wavelength. As expected, correcting the occulter phase becomes less effective when the input beam bandwidth is increased. This simulation predicts that the two different OD profiles ('measured' and 'design' in Fig. 9) of the occulting mask perform about the same when $\Delta\lambda = 80$ nm (10% of the center wavelength). The best simulation result obtainable with the current HEBS occulting mask, our model, and the current DM setting (or correcting phase) is $C_m = 5.3 \times 10^{-9}$ and $C_4 = 2.2 \times 10^{-8}$. It must be pointed out that the occulting mask and the Lyot stop used in this study are not optimized for a broadband operation. Also, a broadband speckle-nulling algorithm has not been developed or implemented in the current optical simulation tool. Hence, several new strategies are now under investigation to improve the occulter broadband properties as well as speckle-nulling algorithm for broadband operation, both of which are hoped to yield better performance in the HCIT.

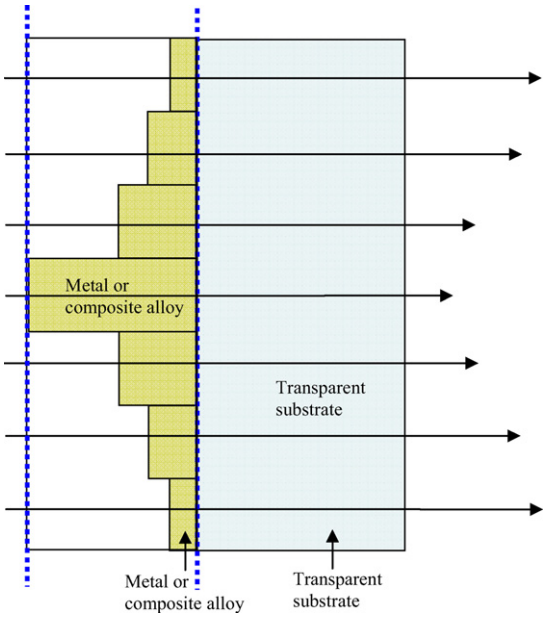

Fig. 12. Concept of a profiled metallic mask; the step heights may be made small enough to produce a continuous profile. Also, a uniform dielectric layer may be applied over the metal layer for protection as well as to fine tune OD vs. wavelength employing interference effects. Similarly, a profiled dielectric layer on either the front or the back side could be applied to flatten the center wavelength phase versus OD.

6. Summary and future directions

Band-limited masks described in this paper have given a great deal of insight to coronagraph architecture. Practical masks fabricated and tested in the HCIT have yielded excellent results with monochromatic light. To obtain similar performance in broadband light, we have undertaken efforts to find alternative materials and techniques to produce masks that exhibit no or little wavelength dependence of OD and phase. It is conceivable that spatially profiled metal masks, as shown conceptually in Fig. 12, may be suitable candidates for image plane masks, if they can be fabricated with adequate accuracy. The phase delay and optical attenuation are required to be independent of wavelength in an adequate bandwidth range, desirably 10 to 20% of the center wavelength. However, common metals exhibit OD and phase dispersion when implemented in thin film form. High reflectivity metals such as Al and Ag present practical fabrication challenges, besides exhibiting poor neutrality with wavelength in transmission. Yet, it is theoretically feasible to design masks with neutral behavior of optical density and phase over a limited bandwidth by employing multiple layers of different metals and dielectrics with controlled spatial thickness profile of each layer; here again practical implementation to the required accuracies is extremely challenging.

Fortunately, our research indicates that certain metals such as Ni and Pt, metallic alloys with Ni, nitrides such as TiAlN, and composite materials with Ni, Cr, Ti and Zr show promise for neutral behavior of OD and phase typically over a 100 nm bandwidth in the visible spectrum. Different materials may have to be chosen for different regions of the spectrum. Theoretical results with several metals, alloys and nano-composites with such characteristics are in preparation for a subsequent paper. Practical design and fabrication of such masks depend critically on the thin film properties which will in turn depend on process conditions. The current state of the art in thin film deposition and monitoring technology allows for layer thickness control to better than $\sim$0.5 nm and hence we hope to produce precisely controlled mask profiles, though significant practical challenges remain.

Our contrast simulation models suggest that, given an OD bias $[\mathrm{OD}_b(\lambda)]$ in the transparent region of the mask, to obtain a mean contrast of 10^{-9} over a 10% bandwidth, the spectral variation of OD, defined as $\Delta\mathrm{OD} = [\{\mathrm{OD}(\lambda) - \mathrm{OD}_b(\lambda)\} - \{\mathrm{OD}(\lambda_0) - \mathrm{OD}_b(\lambda_0)\}]$ for all ODs with λ_0 being the center wavelength in the band, should be less than $\sim$0.01 in the region where mask OD $< \sim$2. Similarly, Δ phase, defined as $[\{\phi(\mathrm{OD}) - \phi(\mathrm{OD}_b)\}_\lambda - \{\phi(\mathrm{OD}) - \phi(\mathrm{OD}_b)\}_{\lambda 0}]$, over the same bandwidth should be less than $\sim$0.01 radian. Tighter tolerances are needed for 10^{-10} contrast. Note that these limits serve as a guidance rather than an absolute requirement because the nature

of variations, for example, linear vs. non-linear dependencies and spatial frequency of the variations, over the band may allow for adjustments in mask profiles as well as in nulling approaches to obtain the best contrast achievable with a particular mask. In such limits, detailed simulations are needed to judge the effectiveness of a specific mask or underlying technology. With layered structures specifically tuned for broadband performance, we hope to produce masks with minimum errors and achieve better than 10^{-9} contrast in 10% bandwidth light, paving the way for further improvements towards 10^{-10} contrast in broadband light.

Acknowledgements

The authors who assembled this manuscript, with the immense work and help of the entire TPF coronagraph team at JPL, are very grateful to their contributions and comments at various stages. They also thank Dr. Wesley Traub of JPL for his encouragement and support for this project. This work was performed at the Jet Propulsion Laboratory, California Institute of Technology, under a contract with the National Aeronautics and Space Administration. Reference herein to any specific commercial product, process or service by trade name, trademark, manufacturer, or otherwise, does not constitute or imply its endorsement by the United States Government or the Jet Propulsion Laboratory, California Institute of Technology.

References

[1] M.J. Kuchner, W.A. Traub, A coronagraph with a band-limited mask for finding terrestrial planets, The Astrophysical Journal 570 (2002) 900–908.
[2] J.W. Goodman, Introduction to Fourier Optics, McGraw–Hill, San Francisco, 1968.
[3] M.J. Kuchner, D.N. Spergel, Terrestrial planet finding with a visible light coronagraph, in: D. Deming, S. Seager (Eds.), Scientific Frontiers in Research on Extrasolar Planets, in: Astronomical Society of the Pacific Conference Series, vol. 294, 2003, pp. 603–610.
[4] O. Lay, J. Green, D. Hoppe, S. Shaklan, Coronagraph mask tolerances for exo-Earth detection, in: D.R. Coulter (Ed.), Techniques and Instrumentation for Detection of Exoplanets II, in: Proceedings of SPIE, vol. 5905, 2005, pp. 148–161.
[5] M.J. Kuchner, J. Crepp, J. Ge, Eighth-order image masks for terrestrial planet finding, The Astrophysical Journal 628 (2005) 466–473.
[6] S. Shaklan, J. Green, Low order aberration sensitivity of eighth order coronagraph masks, The Astrophysical Journal 628 (2005) 474–477.
[7] M.J. Kuchner, A unified view of coronagraph image masks, astro-ph/0401256.
[8] K. Balasubramanian, et al., Occulting focal plane masks for terrestrial planet finder coronagraph—design, fabrication, simulations and test results, in: IAU Colloquium 200 Conference Proceedings, 2006, pp. 405–409.
[9] J.T. Trauger, et al., Coronagraph contrast demonstrations with the High Contrast Imaging Testbed, in: J. Mather (Ed.), Optical, Infrared, and Millimeter Space Telescopes, in: Proceedings of SPIE, vol. 5487, 2004, pp. 1330–1336.
[10] M.J. Kuchner, D.N. Spergel, Notch filter masks: Practical image masks for planet finding coronagraphs, The Astrophysical Journal 594 (2003) 617–626.
[11] Canyon Materials, Inc., San Diego, CA, http://canyonmaterials.com.
[12] J. Crepp, et al., Laboratory testing of a Lyot coronagraph equipped with an eighth-order notch filter image mask, The Astrophysical Journal 646 (2006) 1252–1259.
[13] E. Sidick, D.W. Wilson, Behavior of imperfect band-limited coronagraphic masks in a high-contrast imaging system, Applied Optics 46 (9) (2007) 1397–1407.
[14] P.G. Halverson, et al., Measurement of phase and optical density of TPF coronagraph occulting mask materials, in: R.D. Coulter (Ed.), Techniques and Instrumentation for Detection of Exoplanets II, in: Proceedings of SPIE, vol. 5905, 2005, pp. 59051I1I1-10.
[15] J.T. Trauger, W.A. Traub, A laboratory demonstration of the capability to image an Earth-like extrasolar planet, Nature 446 (2007) 771–773.